

# Level-Set Curvature Neural Networks: A Hybrid Approach

Luis Ángel Larios-Cárdenas<sup>a,\*</sup>, Frédéric Gibou<sup>a,b</sup>

<sup>a</sup>Department of Computer Science, University of California, Santa Barbara, CA 93106

<sup>b</sup>Department of Mechanical Engineering, University of California, Santa Barbara, CA 93106

---

## Abstract

We present a hybrid strategy based on deep learning to compute mean curvature in the level-set method. The proposed inference system combines a dictionary of improved regression models with standard numerical schemes to estimate curvature more accurately. The core of our framework is a switching mechanism that relies on well-established numerical techniques to gauge curvature. If the curvature magnitude is larger than a resolution-dependent threshold, it uses a neural network to yield a better approximation. Our networks are multi-layer perceptrons fitted to synthetic data sets composed of circular- and sinusoidal-interface samples at various configurations. To reduce data set size and training complexity, we leverage the problem’s characteristic symmetry and build our models on just half of the curvature spectrum. These savings result in compact networks able to outperform any of the system’s numerical or neural component alone. Experiments with static interfaces show that our hybrid approach is suitable and notoriously superior to conventional numerical methods in under-resolved and steep, concave regions. Compared to prior research, we have observed outstanding gains in precision after including training data pairs from more than a single interface type and other means of input preprocessing. In particular, our findings confirm that machine learning is a promising venue for devising viable solutions to the level-set method’s numerical shortcomings.

*Keywords:* Level-Set Method, Deep Learning, Mean Curvature

---

## 1. Introduction

Mean curvature is a fundamental interface attribute in free boundary problems [1] for its relation to surface tension in physics [2] and its regularization property in optimization. It plays a crucial role in the solution of numerical models for applications such as multiphase flows [3, 4], image segmentation [5], solidification of multi-component alloys [6], and morphogenesis [7].

One of the most successful numerical schemes for advecting interfaces subject to velocity fields is the level-set method [8–10]. The level-set framework belongs to a family of Eulerian formulations, alongside the volume-of-fluid [11] and the phase-field [12] models. These methods use an implicit function to capture and evolve the interface. The main advantage of Eulerian formulations is their natural ability to handle complex interface topologies. In particular, implicit methods do not need to resort to any complicated procedures to manipulate free boundaries explicitly.

Because of its implicit representation, the level-set method provides a simple relation to computing interface mean curvature. The accuracy of this estimation relies on the smoothness of the level-set function [2]. We can enforce such a smoothness by reinitializing the underlying level-set into a signed distance function with iterative procedures. However, high-order reinitialization schemes do not always lead to satisfactory results, especially in under-resolved regions and non-uniform grids. Our goal is to explore a hybrid strategy that combines inexpensive reinitialization in the level-set method with more recent data-driven technologies.

The last two decades have witnessed a resurgence of machine learning research [13–15] in areas such as image processing (e.g., segmentation [16, 17], classification [18, 19], reconstruction [13, 20], and synthesis [21]), natural language and information retrieval, (e.g., distributed word representations [22–24] and context embeddings [25]), and sequence and advanced language models (e.g., machine language translation [26, 27]). Data availability and widespread access to powerful computing resources have fueled a renewed enthusiasm for this technology in the computer science community and other disciplines like mathematics, physics, and engineering [28].

---

\*Corresponding author: lal@cs.ucsb.edu

Artificial neural networks are computational graphs of elementary units interconnected in some particular way to compute a function of its inputs by using connection weights as intermediate parameters [13]. Supervised neural networks are function approximators [14] capable of capturing a high degree of complexity and non-linearity. These models learn by successively adapting their weights to minimize a loss metric given their current parameters and a training data set. Although training neural networks is a long and expensive process involving backpropagation [13], one does this offline and once for each application. Later, one can use the neural network as a black box to estimate the output for data samples never seen during the learning stage.

Novel research in computational science has incorporated the neural networks' ability to approximate any function. We can trace the use of regression models in this discipline back to the pioneering work of Lagaris *et al.* in [29, 30]. Lagaris and coauthors trained their multi-layer perceptrons to solve initial and boundary problems in ordinary and partial differential equations. More recently, Raissi *et al.* [31, 32] have presented physics-informed neural networks and have constructed neural models to discover dynamic dependencies in spatiotemporal data sets.

Over the past few years, practitioners have also integrated neural networks to the numerical solution of conservation laws as troubled-cell indicators [33]. These models flag near-discontinuity regions where Runge-Kutta discontinuous Galerkin schemes need to be carefully corrected. In that case, robust binary classifiers ensure the numerical methods' cost-efficiency and remove the prescription of any problem-dependent parameters associated with traditional troubled-cell identifiers. Similarly, Morgan *et al.* [34] have trained a shock detector coupled with a high-order Lagrangian hydrodynamic method in complex flows. The idea is to use a first-order solution in cells lying near a shock and a high-order solution everywhere else in the mesh. The intention is to avoid treating smooth flow features as shocks, which could lead to reduced accuracy.

Last, computational fluid dynamics researchers have started to inspect machine learning to address challenging tasks in the volume-of-fluid method (or VOF). In [35], Després and Jourdain have proposed a family of VOF-machine learning algorithms suitable to bi-material compressible Euler calculations. Their development includes training a five-layered network with lines, arcs, and corners. Després and Jourdain have implemented their regression model in a finite volume Lagrange+remap solver, aiming at an accurate transport/remap of reconstructed interfaces. In like manner, Qi *et al.* [36] have pioneered a machine learning strategy to reduce the complexity and improve the accuracy of interface curvature calculations in two-dimensional VOF schemes. In [36], a neural network ingests (nine-cell stencil) volume fractions and produces continuous dimensionless curvature values for center cells. To train their neural model, Qi and coauthors used large synthetic data sets, spanning a wide range of curvatures from circular interfaces. A more recent and detailed work by Patel *et al.* [37] has addressed local curvature estimation in three-dimensional VOF schemes. Their approach has proven effective in standard test cases with multiple bubble simulations. Patel and colleagues have shown that their solver outperforms the convolution method and even matches the precision of the height function method. In a parallel VOF study, Ataei *et al.* [38] have proposed a multi-layer perceptron to carry out piece-wise linear interface construction (or PLIC). Their approach has reduced computational costs and surpassed the quality of the analytical and iterative traditional PLIC when approximating the location of moving boundaries.

The present research is motivated by the recent progress in [36, 37] and extends the deep learning strategy introduced in [39] to compute mean curvature in the level-set method. Our work aligns in spirit with the cost-efficiency goal of [34] too; we seek to incorporate machine learning approximations only when deemed necessary. The proposed hybrid inference system combines a dictionary of regression models with standard numerical schemes to estimate mean curvature more accurately for two-dimensional interfaces. We fit our neural networks to synthetic data sets composed of circular- and sinusoidal-interface samples at various configurations. Further, to reduce data set size and training complexity, we leverage the problem's characteristic symmetry and build our models on just half of the curvature spectrum. These savings result in compact networks able to outperform any of the system's numerical or neural component alone. Experiments with static, smooth interfaces show that our hybrid framework is suitable and notoriously superior to conventional numerical methods in under-resolved and steep, concave interface regions. Compared to the early developments in [39], we have observed outstanding gains in precision after including training data pairs from more than a single interface type and other means of input preprocessing. In particular, our findings confirm that machine learning is a promising venue for devising viable solutions to the level-set method's numerical shortcomings.

We have organized the present report as follows. Section 2 summarizes the level-set method. Next, section 3 gives a thorough description of our hybrid strategy and how to design the improved level-set curvature neural networks. We devote section 4 to experiments and results, and section 5 draws some conclusions and opportunities for future work.

## 2. The Level-Set Method

The level-set method [8] is an Eulerian formulation that defines an arbitrary interface of a domain,  $\Omega \subseteq \mathbb{R}^n$ , by  $\Gamma \doteq \{\mathbf{x} : \phi(\mathbf{x}) = 0\}$  and its interior and exterior regions by  $\Omega^- \doteq \{\mathbf{x} : \phi(\mathbf{x}) < 0\}$  and  $\Omega^+ \doteq \{\mathbf{x} : \phi(\mathbf{x}) > 0\}$ , where  $\phi(\mathbf{x}) : \mathbb{R}^n \mapsto \mathbb{R}$  is a Lipschitz continuous function known as the *level-set function*.

Provided that  $\phi(\mathbf{x})$  remains smooth after advection, it is straightforward to compute mean curvature,  $\kappa(\mathbf{x})$ , at any point  $\mathbf{x} \in \Omega$  as

$$\kappa(\mathbf{x}) = \nabla \cdot \frac{\nabla \phi(\mathbf{x})}{|\nabla \phi(\mathbf{x})|}, \quad (1)$$

where  $\nabla \phi(\mathbf{x})$  is discretized with second-order accurate central differences.

In practice,  $\phi(\mathbf{x})$  gets periodically reinitialized into a signed distance function to the interface [3] by solving the equation

$$\phi_\tau + S(\phi^0)(|\nabla \phi| - 1) = 0, \quad (2)$$

where  $\tau$  represents pseudo time,  $\phi^0$  is the level-set function before reshaping, and  $S(\phi^0)$  is a smoothed-out signum function. Reinitialization helps to produce robust numerical results and simplifies computations [40]. As shown in [39], redistancing has also been linked to seamless neural network training and improved accuracy when estimating mean curvature along smooth interfaces. For a complete description of the level-set method and its applications, we refer the interested reader to the classic text by Osher and Fedkiw [9] and the recent review by Gibou *et al.* [10].

## 3. Methodology

The present work builds on the findings and lessons learned from prior research in [39], which applied deep learning to compute mean curvature in the level-set method. The results in [39] showed that, unlike machine learning and volume-of-fluid methods [36, 37], the level-set framework required more complex supervised neural networks to approximate curvature values. Also, training with samples collected from circular interfaces did not yield more accurate estimations than a multi-step numerical approach. Here, we explore several ways to increase the curvature regression models' accuracy by training with distinct classes of interfaces and data augmentation [13, 15]. Besides, we exploit machine learning techniques for input preprocessing [41] and reduce the neural networks' spatiotemporal footprint by taking advantage of the problem's intrinsic symmetry.

The machine learning approach we are about to introduce relies on building a dictionary for mapping domain resolutions to neural networks. Our goal is to reduce the complexity of the problem at hand by breaking it into more manageable components [39]. Assuming that the computational domain,  $\Omega$ , has been discretized into the smallest local mesh size  $h = \Delta x = \Delta y$ , we design and test *level-set curvature neural networks* that fit only to that nodal spacing. These neural networks are suitable for regular and adaptive grids (see [42–44]). We remark that we have resolved our computational domains with quad-trees [45] for training and testing. Such a discretization speeds up data set construction significantly when the level-set function does not have an analytic form that one can use on large grids.

As seen in Figure 1, a curvature neural network is a supervised multi-layer perceptron, trained on a synthetic data set,  $\mathcal{D}$ . To assemble  $\mathcal{D}$ , we extract samples from *circular-* and *sinusoidal-interface* level-set functions embedded in two-dimensional domains. By varying the configuration of such interfaces, one can construct a rich collection of patterns that associate level-set function values to dimensionless mean curvatures. A learning sample or data pair is a tuple  $(\phi, h\kappa)_{i,j}$ , where

$$\phi \doteq \begin{pmatrix} \phi_{i-1,j+1}, & \phi_{i,j+1}, & \phi_{i+1,j+1}, \\ \phi_{i-1,j}, & \phi_{i,j}, & \phi_{i+1,j}, \\ \phi_{i-1,j-1}, & \phi_{i,j-1}, & \phi_{i+1,j-1} \end{pmatrix} \in \mathbb{R}^9 \quad (3)$$

is an array of level-set values from the standard 9-point stencil centered at node<sup>1</sup>  $(i, j)$ .  $h\kappa$  is the corresponding dimensionless curvature at the nearest point,  $\mathbf{x}_{i,j}^\perp$ , on the interface,  $\Gamma$ . Figure 2 contains a schematic of  $\phi$  and the location where we compute  $h\kappa$ . As the diagram shows, we optimize our curvature neural models to infer  $h\kappa$  at  $\Gamma$  for any node  $(i, j)$  that satisfies at least one of the four conditions:  $\phi_{i,j} \cdot \phi_{i\pm 1,j} \leq 0$  or  $\phi_{i,j} \cdot \phi_{i,j\pm 1} \leq 0$ .

<sup>1</sup>We use the terms node, vertex, and grid point as synonyms.

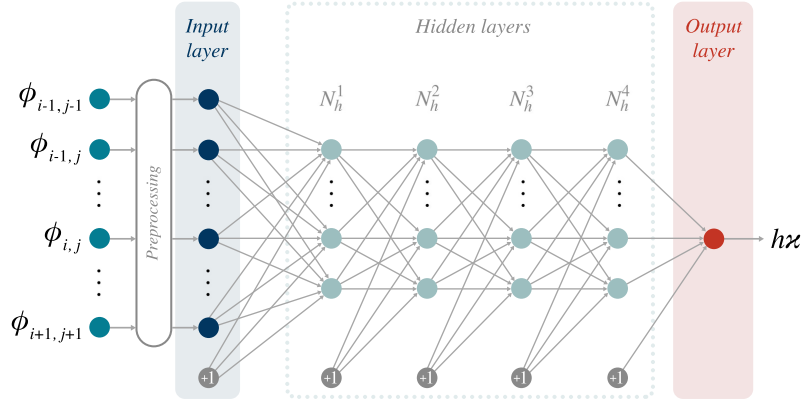


Figure 1: General architecture of a level-set curvature neural network. The input is a nine-dimensional array of preprocessed level-set function values. Each hidden layer has  $N_h^i$  ReLU units ( $1 \leq i \leq 4$ ), and the output layer contains a single linear neuron that produces the dimensionless curvature,  $h\kappa$ .

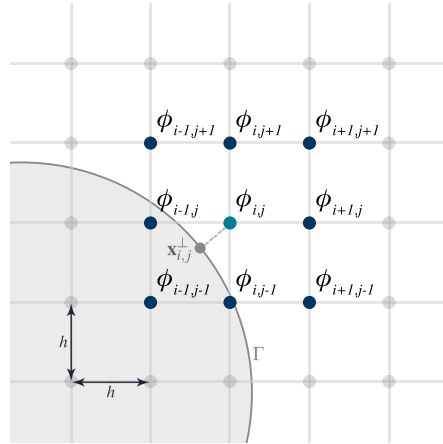


Figure 2: Nine-point stencil of node  $(i, j)$  adjacent to the interface and the level-set function values involved in the numerical and neural estimation of mean curvature.

### 3.1. Circular-Interface Data Set Generation

The procedure for collecting learning samples from level-set functions with circular interfaces resembles the method outlined in [36] and [39]. Here, however, we introduce another approach for spacing out circles across the domain and ensure that all discrete curvatures are sampled equally. The latter is known, among pattern recognition practitioners, as *constructing balanced data sets*. The goal is to provide each target class with the same probability of being accounted for by the learning algorithm. To achieve this, we do not collect samples from a fixed number of circular interfaces with the same radius [39]. Instead, we explicitly set the number of data pairs that we must extract for every discrete radius. This technique increases the visibility of high-curvature data pairs (i.e., from small-radius circles); had we not done that, such samples would be under-represented given that low-curvature patterns can quickly become dominant.

Let  $\mathcal{D}_c$  be the set of data pairs extracted from bivariate functions,  $\phi(\mathbf{x}) : \mathbb{R}^2 \mapsto \mathbb{R}$ , characterized by smooth circular isocontours. Define the level-set functions

$$\phi_{sdf}^c(x, y) = \sqrt{(x - x_0)^2 + (y - y_0)^2} - r \quad \text{and} \quad \phi_{rls}^c(x, y) = (x - x_0)^2 + (y - y_0)^2 - r^2, \quad (4)$$

where  $(x_0, y_0)$  is the center of the circular interface, and  $r$  is the radius. Notice that unlike  $\phi_{sdf}^c(x, y)$ ,  $\phi_{rls}^c(x, y)$  is not a signed distance function. Thus, one must reinitialize  $\phi_{rls}^c(x, y)$  after evaluating the level-set function on the discretized domain. We have chosen ten iterations throughout this work to solve equation (2) numerically. This choice

---

**Algorithm 1:** Data set generation from circular-interface level-set functions.

---

**Input:** mesh size,  $h$ ; minimum curvature,  $\kappa_{min}$ ; maximum curvature,  $\kappa_{max}$ .

**Result:** data set with samples from circular interfaces,  $\mathcal{D}_c$ .

```
1  $h_{base} \leftarrow 2^{-7}$ ; // Reference mesh size
2  $r_{min} \leftarrow 1/\kappa_{max}$ ; // Minimum and maximum radii
3  $r_{max} \leftarrow 1/\kappa_{min}$ ;
4  $\kappa_{flat} = 10\kappa_{min}$ ; // Minimum curvature and radius to trigger neural inference
5  $r_{flat} \leftarrow 1/\kappa_{flat}$ ;
6  $N_r \leftarrow \left\lceil 2 \left( \frac{r_{max}-r_{min}}{h_{base}} + 1 \right) \left( \log_2 \left( \frac{h_{base}}{h} \right) + 1 \right) \right\rceil$ ; // Number of distinct radii
7  $N_s \leftarrow \left\lceil \frac{5\pi}{h^2} \left( r_{flat}^2 - (r_{flat} - h)^2 \right) \right\rceil$ ; // Potential number of samples per radius
8  $\bar{N}_s \leftarrow \left\lceil \frac{5\pi}{h_{base}^2} \left( r_{flat}^2 - (r_{flat} - h_{base})^2 \right) \right\rceil$ ; // Allowable samples per radius
9  $\mathcal{D}_c \leftarrow \emptyset$ ;
   // Evaluate  $N_r$  radii computed from equally-spaced curvature values  $\kappa \in [\kappa_{min}, \kappa_{max}]$ 
10 foreach curvature  $\kappa$  in  $\text{LinSpace}(\kappa_{min}, \kappa_{max}, N_r)$  do
11    $r \leftarrow 1/\kappa$ ; // Current radius
   // Data sets for exact signed-distance and reinitialized level-set functions
12    $\mathcal{S}_{sdf} \leftarrow \emptyset, \mathcal{S}_{rls} \leftarrow \emptyset$ ;
13   while  $|\mathcal{S}_{sdf}| < N_s$  do // Collect samples for current radius
14      $(x_0, y_0) \sim \mathcal{U}(-h/2, +h/2)$ ; // Random circle's center around origin
15      $\phi_{sdf}^c \leftarrow \text{LevelSetSDF}(x_0, y_0, r)$ ; // Build exact and reinitialized level-set functions
16      $\phi_{rls}^c \leftarrow \text{LevelSet}(x_0, y_0, r)$ ;
17     set up computational domain,  $\Omega$ , with proper bounds;
18     evaluate  $\phi_{sdf}^c$  and  $\phi_{rls}^c$  on discretization of  $\Omega$ ;
19     reinitialize  $\phi_{rls}^c$  using 10 iterations;
20     foreach node  $n$  along  $\Gamma$  do
21       build pairs  $-(\phi_{sdf}^c, h\kappa)$  and  $-(\phi_{rls}^c, h\kappa)$  from the stencil of  $n$ ;
22       add samples to  $\mathcal{S}_{sdf}$  and  $\mathcal{S}_{rls}$ 
23     end
24   end
   // Extract  $\bar{N}_s$  samples from  $\mathcal{S}_{sdf}$  and  $\mathcal{S}_{rls}$  and add them to  $\mathcal{D}_c$ 
25    $\mathcal{D}_c \leftarrow \mathcal{D}_c \cup \text{RandomSamples}(\mathcal{S}_{sdf}, \bar{N}_s)$ ;
26    $\mathcal{D}_c \leftarrow \mathcal{D}_c \cup \text{RandomSamples}(\mathcal{S}_{rls}, \bar{N}_s)$ ;
27 end
```

---

has resulted in a cheap redistancing process that guarantees enough smoothness in the level-set function. As pointed out by the authors in [39], reinitialization plays a couple of important roles when training level-set curvature neural networks. First, it removes unstructured noise that could worsen architectural complexity and undermine the neural model's accuracy. Second, neural networks can improve their interpolative power if one includes reinitialized values and exact signed distances to  $\Gamma$ . Such an improvement is possible because the regression model can better assimilate connections between noiseless data pairs and their reinitialized versions when both share the same  $h\kappa$  output.

Algorithm 1 describes how to construct  $\mathcal{D}_c$  in great detail. In the present work, we feed the process with minimum and maximum mean curvature values of  $\kappa_{min} = \frac{1}{2}$  and  $\kappa_{max} = 85\frac{1}{3}$ . Also, depending on the experimental conditions, one defines the mesh size,  $h$ , and a limiting curvature,  $\kappa_{flat}$ , used for discriminating flat regions and preventing data explosion. We will come back with more information about  $\kappa_{flat}$  later in Section 3.3 once we introduce our hybrid approach. After setting these constants, generating the data pairs  $(\phi, h\kappa)$  boils down to deciding how many to collect along  $\Gamma$  and how to distribute the interfaces across the computational domain.

We begin by specifying the number of unique radii,  $N_r$ . This is necessary to define the level-set functions in equation (4). Intuitively,  $N_r$  should be proportional to the mesh size  $h$ ; however, such a number could become prohibitive as  $h \rightarrow 0$ . We circumvent this issue by expressing  $N_r$  in terms of a base resolution,  $h_{base}$ , and requiring a linear growth rather than exponential. As for the number of samples,  $N_s$ , to collect for each interface radius, we approximate it with

the area difference between the circle with radius  $\kappa_{flat}^{-1}$  and the following circle whose radius is  $(\kappa_{flat} - h)^{-1}$ . Notice we have opted for a radius smaller than  $\kappa_{min}^{-1}$  to avoid overproducing data pairs. Afterward, we only keep a random subset of size  $\bar{N}_s$  to further bound the training population. This whole system guarantees that, at least for  $\mathcal{D}_c$ , each discrete  $\kappa$  value is equally probable of being observed during training.

Next, one must resolve how to space out  $N_r$  unique radii across  $\Omega$ . Unlike [36] and [39], we compute such radii from uniform curvature values between  $\kappa_{min}$  and  $\kappa_{max}$ . The rationale for this choice abides by the balanced data set principle; had we chosen to calculate  $\kappa$  from equidistant radii, we would have gotten the target dimensionless curvature distribution in  $\mathcal{D}_c$  overly skewed near zero.

Algorithm 1 also shows how to introduce randomness into  $\mathcal{D}_c$  when defining the level-set functions  $\phi_{sdf}^c(x, y)$  and  $\phi_{rls}^c(x, y)$ . To do this, we perturb the circles' centers about the origin of  $\Omega$  with a uniform random value between  $-h/2$  and  $+h/2$ . This simple form of data augmentation has proven effective in enhancing the generalization of other inference systems, such as image classifiers and convolutional networks [13, 15]. In our approach, we repeatedly generate random interface centers until the expected number of samples is satisfied.

Last, we state a subtle yet crucial property of the curvature problem that one can leverage in data set construction and neural network design. Namely, if one can estimate  $h\kappa$  (with a neural or numerical solver) from the stencil of level-set values  $\phi$ , then  $-\phi$  produces  $-h\kappa$  under the same scheme. It then suffices to store the negated stencils and their dimensionless curvatures, incurring no information loss. This technique has been beneficial to our proposed framework for two reasons: it favors time-space efficiency, and it suits and improves the quality of the neural network fitting process.

### 3.2. Sinusoidal-Interface Data Set Generation

Besides training on circular-interface samples, we also consider data pairs,  $(\phi, h\kappa)$ , extracted from level-set functions characterized by smooth sinusoidal zero isocontours. Compared to prior research [39], this has helped improve our proposed curvature neural networks' accuracy, as shown in Section 4.

Let  $\mathcal{D}_s$  be the set of learning data pairs collected from bivariate functions,  $\phi(\mathbf{x}) : \mathbb{R}^2 \mapsto \mathbb{R}$ , whose zero level sets are expressed as

$$f_s(t) = A \sin(\omega t), \quad (5)$$

where  $A$  is the wave amplitude, and  $\omega$  is the sinusoidal frequency. Unlike equation (4), however, there is no readily available formula,  $\phi(x, y)$ , that resembles a signed distance function and produces the above sinusoidal interface. We address this limitation by parametrizing and discretizing  $f_s(t)$  into line segments. This strategy is similar to how animators control the motion of points along curves [46]. After discretization is complete, we define the level-set function

$$\phi_{rls}^s(x, y) = \begin{cases} -d_s(x, y), & y > f_s(x) \\ +d_s(x, y), & y < f_s(x) \\ 0, & y = f_s(x) \end{cases}, \quad (6)$$

where  $d_s(x, y)$  is the shortest distance between  $(x, y)$  and the closest line segment on the interface. Notice that  $\Gamma$  splits the computational domain,  $\Omega$ , into negative and positive regions depending on whether a node lies above or below  $f_s(x)$  (see Figure 3a). We adopt this configuration because it ensures curvature comes up positive along convex portions of the negative domain. This choice also agrees with the analytic expression that yields the sine wave's signed curvature:

$$\kappa_s(t) = -\frac{A\omega^2 \sin(\omega t)}{(1 + A^2\omega^2 \cos^2(\omega t))^{3/2}}. \quad (7)$$

Given a node  $(i, j)$  with coordinates  $\mathbf{x}_{i,j} = (x_i, y_i)$  next to the interface, we apply bisection followed by Newton-Raphson's root finding to recover the optimal  $t^*$  that produces  $\mathbf{x}_{i,j}^+$  in Figures 2 and 3a. Once  $t^*$  is available, we compute the target curvature with equation (7). Like with  $\phi_{rls}^c(x, y)$  in equation (4), we still require ten iterations to reinitialize the corresponding non-signed distance function  $\phi_{rls}^s(x, y)$ . The latter is guaranteed to turn out well-regularized as long as one discretizes  $f_s(t)$  with sufficiently small parameter intervals,  $\Delta t < h$ .

Specifying the sinusoidal-interface exact signed distance function,  $\phi_{sdf}^s(x, y)$ , relies entirely on numerical optimization for computing the shortest distance from grid points to  $\Gamma$ . Then again, for each node  $(i, j)$  next to the interface, the

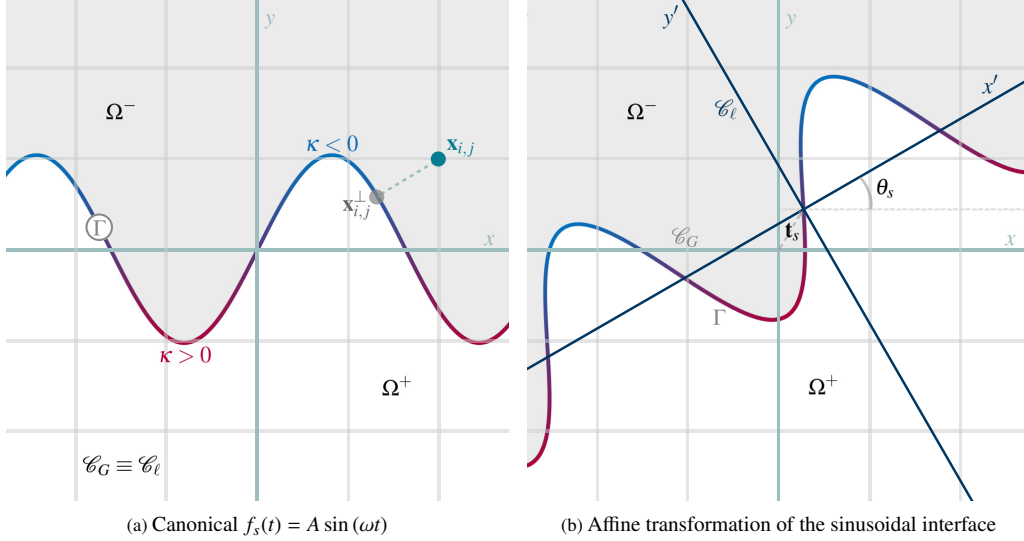


Figure 3: The sinusoidal interface,  $f_s(t)$ , its local coordinate system,  $\mathcal{C}_\ell$ , and the partitioning of the computational domain into negative ( $\Omega^-$ ) and positive ( $\Omega^+$ ) regions.

optimal parameter  $t^*$  that determines  $\mathbf{x}_{i,j}^\perp$  is used to compute  $\kappa_s(t)$  as expressed in equation (7). This process allows us to assemble signed-distance data pairs alongside their reinitialized level-set versions from  $\phi_{rls}^s(x, y)$  to make up  $\mathcal{D}_s$ .

**Remark:** An alternative method to generate reinitialized sinusoidal-interface samples involves “redistancing” the signed distance function  $\phi_{sdf}^s(x, y)$ . This process works because reinitialization introduces numerical perturbations that our algorithm can interpret as noisy inputs. Depending on the mesh size, it is often faster to produce reinitialized data this way than parametrizing  $\Gamma$  to find distances iteratively.

One can manipulate the shape parameters  $A$  and  $\omega$  in equation (5) to generate a wide variety of relationship patterns between  $\phi$  and  $h\kappa$ . However, greater diversification is possible if, besides amplitude and frequency, we also perturb the local frame of the sinusoidal interface. Figure 3b depicts this class of data augmentation, which comprises the translation and rotation of the interface coordinate system,  $\mathcal{C}_\ell$ . To do this, we could redefine the level-sets  $\phi_{sdf}^s(x, y)$  and  $\phi_{rls}^s(x, y)$  in a way that they would take a translation vector,  $\mathbf{t}_s = (x_0, y_0)$ , and a rotation angle,  $\theta_s$ , as additional inputs. In practice, estimating distances from points to the simpler, canonical function  $f_s(t)$  remains unaltered even when  $\mathbf{t}_s$  and  $\theta_s$  are present. To illustrate this idea, let  $\mathcal{C}_G$  be the global coordinate system, and let  $T(\cdot, \cdot)$  and  $R(\cdot)$  be  $3 \times 3$  translation and rotation matrices in homogeneous coordinates [46, 47]. We claim that if  ${}_G M_\ell = R(\theta_s)T(x_0, y_0)$  is an affine transformation that maps points from the local to the global coordinate system, then  ${}_\ell M_G = {}_G M_\ell^{-1} = T(-x_0, -y_0)R^T(\theta_s)$  maps points in the reverse direction: from  $\mathcal{C}_G$  to  $\mathcal{C}_\ell$ . Suppose that we express the point  $\mathbf{x}_G = (x_G, y_G)^T$  in terms of  $\mathcal{C}_G$ , then

$$\mathbf{x}_\ell = \begin{pmatrix} x_\ell \\ y_\ell \end{pmatrix} = \begin{pmatrix} \cos \theta_s (x_G - x_0) + \sin \theta_s (y_G - y_0) \\ \cos \theta_s (y_G - y_0) + \sin \theta_s (x_0 - x_G) \end{pmatrix} \quad (8)$$

are the coordinates of  $\mathbf{x}_G$  with respect to the local coordinate system,  $\mathcal{C}_\ell$ . Having  $\mathbf{x}_\ell = (x_\ell, y_\ell)^T$  at hand, one can evaluate  $\phi_{sdf}^s$  and  $\phi_{rls}^s$ , as usual, to find  $t^*$  and compute the exact distance and curvature at the closest point on  $\Gamma$ .

The procedure to construct  $\mathcal{D}_s$  is combinatorial with some internal, random mechanisms and post-processing steps that fight data explosion. Algorithm 2 summarizes the strategy for collecting samples from sinusoidal-interface level-set functions. The parameters one can vary to produce different boundary configurations are amplitude,  $A$ , frequency,  $\omega$ , displacement,  $\mathbf{t}_s$ , and tilt,  $\theta_s$ . These depend on the minimum and maximum target curvatures,  $\kappa_{min} = \frac{1}{2}$  and  $\kappa_{max} = 85\frac{1}{3}$ , and the computational mesh size,  $h$ . Unlike Algorithm 1, however, we cannot rely on a reference mesh size alone to curb data production. One must be more careful with sinusoidal interfaces at all times because flat regions dominate every single parameter choice.

At the outermost layer, we evaluate the amplitude,  $A$ , over the range of  $[1.5h, 0.25]$ , with a number,  $N_a$ , of equally spaced values. In the following layer, we define the sinusoidal frequency,  $\omega$ , which comes from the range of  $[\omega_{min}, \omega_{max}]$ . This interval guarantees that the maximum (absolute) curvature along the crests lies between  $\frac{\kappa_{max}}{4}$  and  $\kappa_{max}$ . The number of discrete frequency steps,  $N_\omega$ , is proportional to the  $t$ -distance between two consecutive maximal

---

**Algorithm 2:** Data set generation from sinusoidal-interface level-set functions.

---

**Input:** mesh size,  $h$ ; minimum curvature,  $\kappa_{min}$ ; maximum curvature,  $\kappa_{max}$ .

**Result:** data set with samples from sinusoidal interfaces,  $\mathcal{D}_s$ .

```
1  $h_{base} \leftarrow 2^{-7}$ ; // Reference mesh size
2  $L_p = 1 + \frac{\log_2(h_{base}/h)}{3}$ ; // Linear proportion as  $h$  varies from  $h_{base}$  to  $2^{-10}$ 
3  $N_a \leftarrow 33$ ; // Number of distinct amplitudes
4  $A_{min} \leftarrow 1.5h$ ,  $A_{max} \leftarrow 0.25$ ; // Amplitude bounds
5  $N_\theta \leftarrow 34$ ; // Number of distinct tilts of sine's main axis
6  $\theta_{min} \leftarrow -\pi/4$ ,  $\theta_{max} \leftarrow \pi/4$ ; // Tilt bounds
7  $\mathcal{D}_s \leftarrow \emptyset$ ;

// Evaluate  $N_a$  equally-spaced sine amplitudes  $A \in [A_{min}, A_{max}]$ 
8 foreach amplitude  $A$  in  $\text{LinSpace}(A_{min}, A_{max}, N_a)$  do
    // We want to vary  $\max(\kappa)$  for current amplitude  $A$  between  $\kappa_{max}/4$  and  $\kappa_{max}$ 
9      $\omega_{max} \leftarrow \sqrt{\frac{\kappa_{max}}{A}}$ ,  $\omega_{min} \leftarrow \sqrt{\frac{\kappa_{max}}{4A}}$ ; // Frequency range
10     $\mu_{\max(\kappa)} \leftarrow \frac{1}{2} \left( \frac{\kappa_{max}}{4} + \kappa_{max} \right)$ ; // Midpoint between  $\max(\kappa)$  lower and upper bounds
11     $d_{crests} \leftarrow \frac{\pi}{2} \left( \frac{1}{\omega_{min}} - \frac{1}{\omega_{max}} \right)$ ; // Distance between consecutive t-values with  $\pm$ crests
12     $N_\omega \leftarrow \left\lceil \frac{d_{crests}}{h_{base}} L_p \right\rceil + 1$ ; // Number of distinct frequency values

    // Evaluate  $N_\omega$  equally-spaced sine frequencies  $\omega \in [\omega_{min}, \omega_{max}]$ 
13    foreach frequency  $\omega$  in  $\text{LinSpace}(\omega_{min}, \omega_{max}, N_\omega)$  do
        // Data sets for exact signed-distance and reinitialized level-set functions
14         $\mathcal{S}_{sdf} \leftarrow \emptyset$ ,  $\mathcal{S}_{rls} \leftarrow \emptyset$ ;

        // Evaluate  $N_\theta - 1$  equally spaced sine tilts  $\theta_s \in [\theta_{min}, \theta_{max})$ 
15        foreach tilt  $\theta_s$  in  $\text{LinSpace}(\theta_{min}, \theta_{max}, N_\theta)$ , except  $\theta_{max}$  do
             $(x_0, y_0) \sim \mathcal{U}(-h/2, +h/2)$ ; // Random translation of  $\mathcal{C}_\ell$ 
16             $\phi_{sdf}^s \leftarrow \text{LevelSetSDF}(A, \omega, \theta_s, x_0, y_0)$ ; // Build exact and reinitialized
17             $\phi_{rls}^s \leftarrow \text{LevelSet}(A, \omega, \theta_s, x_0, y_0)$ ; // level-set functions
18            set up computational domain,  $\Omega \equiv [-0.5, 0.5]^2$ ;
19            evaluate  $\phi_{sdf}^s$  and  $\phi_{rls}^s$  on discretized  $\Omega$ ;
20            reinitialize  $\phi_{rls}^s$  using 10 iterations;

21            foreach node  $n$  along  $\Gamma$  do
22                compute  $n$ 's target  $\kappa$  using the transformed sinusoidal interface  $f_s(t) = A \sin(\omega t)$ ;
23                if  $|\kappa| < \kappa_{min}$  then skip  $n$  as  $\kappa$  belongs to a flat region ;
24                // Take samples from  $n$  with an ease-in probability from 0.05 to 1
                // where  $\Pr(|\kappa| \geq \mu_{\max(\kappa)}) = 1$  and  $\Pr(|\kappa| = 0) = 0.05$ 
25                if  $\mathcal{U}(0, 1) < 0.05 + 0.95 * \text{EaseIn}(|\kappa|/\mu_{\max(\kappa)})$  then
26                    build pairs  $(-1)^{\kappa/|\kappa|}(\phi_{sdf}^s, h\kappa)$  and  $(-1)^{\kappa/|\kappa|}(\phi_{rls}^s, h\kappa)$  from the stencil of  $n$ ;
27                    augment samples by rotating the stencils of input level-set values by  $90^\circ$ , three times;
28                    add augmented samples to  $\mathcal{S}_{sdf}$  and  $\mathcal{S}_{rls}$ 
29                end
30            end
31        end
32         $\mathcal{D}_s \leftarrow \mathcal{D}_s \cup \mathcal{S}_{sdf} \cup \mathcal{S}_{rls}$ ; // Accumulate samples in output set
33    end
34 end
```

---

$|f(t)|$  values and inversely proportional to the reference mesh size,  $h_{base}$ . Further,  $N_\omega$  is scaled by a constant,  $L_p$ , which increases linearly with  $h$  to account for smaller local cell widths.

After choosing  $A$  and  $\omega$ , we perturb the local reference frame,  $\mathcal{C}_\ell$ , that embeds the canonical sinusoidal interface (5). This task begins by varying the tilt,  $\theta_s$ , over the range of  $[-\pi/4, +\pi/4]$ , with  $N_\theta$  uniform values. Next, the displacement,  $\mathbf{t}_s = (x_0, y_0)$ , is extracted from a uniform random distribution whose lower and upper bounds are  $-h/2$  and  $+h/2$ . Notice

the latter matches the perturbation method used to instantiate the circular interfaces in Section 3.1. Having thus defined all the interface shape and transformation parameters, we prepare the level-sets in equation (6) and sample them on the discretized computational domain. As in Algorithm 1, the data pairs in  $\mathcal{D}_s$  come from exact signed distance functions and their reinitialized level-set versions.

The following step in Algorithm 2 involves analyzing nodes along  $\Gamma$  and deciding whether we should add their data pairs to  $\mathcal{D}_s$  or discard them. We seek to prioritize steep curvatures over flat ones to build a balanced data set as much as possible. First, we filter out any vertex  $(i, j)$  if its projection,  $\mathbf{x}_{i,j}^\perp$ , belongs in a sufficiently planar region ( $|\kappa| < \kappa_{min}$ ). If the target  $|\kappa|$  at the boundary is above the threshold  $\mu_{\max(\kappa)} = \text{mean}\left(\frac{1}{4}\kappa_{max}, \kappa_{max}\right)$ , we keep the grid point. For the remaining candidate nodes, we use an ease-in [46] cumulative distribution function to determine if they should be part of  $\mathcal{D}_s$ . This probability depends on the ratio  $|\kappa|/\mu_{\max(\kappa)}$  and ensures that high curvatures are more likely to make it to the last step. Next, we assemble the pairs  $(-1)^{\kappa/|\kappa|}(\phi, h\kappa)$  for the selected vertices, restating that we always store the negative versions of the level-set and mean curvature values. Last, we resort to extra data augmentation by rotating each stencil,  $\phi$ , by  $90^\circ$ , up to three times. This technique is not uncommon when training image classifiers [15], and we have introduced it in our treatment of sinusoidal-interface samples to enhance model generalization.

Experience has shown that despite the probabilistic approach described above, the  $\kappa$  distribution in  $\mathcal{D}_s$  tends to get skewed near  $-\kappa_{min}$ . To mitigate this problem, we perform a second round of random selection with *sample binning*. The procedure is simple. First, the elements in  $\mathcal{D}_s$  get organized into a histogram with 20 or 40 containers. The grouping criterion is the dimensionless curvature. Next, one finds the size,  $N_b$ , of the bin with the smallest number of data pairs. Then, we sub-sample any bin of size larger than  $K \cdot N_b$ , for  $K = 2, 3.5$ , (with no replacement) until the number of points in it does not exceed  $K \cdot N_b$ . This makes sure that the target curvature histogram of  $\mathcal{D}_s$  looks more or less rectangular.

After the circular- and sinusoidal-interfaces data sets are complete, we combine them into  $\mathcal{D} = \mathcal{D}_c \cup \mathcal{D}_s$  and continue to train a dedicated neural network for the selected mesh size.

### 3.3. Level-Set Curvature Neural Networks and the Hybrid Approach

Our neural networks are black-box models,  $F_h(\cdot) : \mathbb{R}^9 \mapsto \mathbb{R}$ , that output the dimensionless curvature,  $h\kappa$ , of smooth interfaces in  $\mathbb{R}^2$ , given a nine-dimensional input vector of nodal level-set function values,  $\phi$ . These feed-forward models call for conventional network training, as in [39], but here we propose a simplified procedure. Our strategy exploits the advantage of efficient numerical methods to increase accuracy and reduce topological complexity.

Earlier, we established the intrinsic symmetry property of the curvature computation problem. This feature helped us save space since  $\mathcal{D}$  was required to maintain information related to only negative curvature samples. Now, we hypothesize that a network trained on such a half spectrum has the same or higher expressive power than a model that handles negative and positive curvature samples. This claim hinges on the availability of an inexpensive, reliable method to infer the curvature sign from the values in  $\phi$ . The numerical framework we are trying to improve on meets the requirements for a good sign indicator in all respects and more.

An attractive advantage of numerical level-set methods is that they provide the simple relation (1) for calculating  $\kappa$  to any order of accuracy. However, it is easy to see that the discretization of equation (1) defines mean curvature everywhere in  $\Omega$  but not precisely at  $\Gamma$ , where it is needed the most. This problem has been linked to certain limitations when considering the well-balanced property of traditional level-set schemes [2]. Interpolation and distance-weighted average are standard formulations often used to circumvent this deficiency and approximate curvatures closer to their expected values at the interface. Therefore, as in [39], we have adopted a *compound numerical method* for computing mean curvature. In this approach, the second-order, central finite difference discretization of equation (1) is followed by bilinear interpolation at the location

$$\mathbf{x}_{i,j}^\Gamma = \mathbf{x}_{i,j} - \phi_{i,j} \frac{\nabla\phi(\mathbf{x}_{i,j})}{|\nabla\phi(\mathbf{x}_{i,j})|}, \quad (9)$$

where  $\mathbf{x}_{i,j}^\Gamma$  is a rough estimation of  $\mathbf{x}_{i,j}^\perp$ , and  $\phi_{i,j}$  is the level-set value of node  $(i, j)$  next to  $\Gamma$  (see Figure 2).

Let  $F_h(\cdot)$  be a multi-layer perceptron optimized for producing (negative) dimensionless curvature values in a computational domain with mesh size  $h$ . Our proposed *hybrid inference approach* (Algorithm 3) is a decision-based process that combines the two-step numerical method and  $F_h(\cdot)$  to estimate  $\kappa$  at the interface. It uses the compound numerical method as a first-level mechanism to gauge the interface curvature and trigger the neural network evaluation only if deemed necessary. When the latter holds, the initial numerical approximation determines if the input stencil belongs in a convex or concave region. Depending on this, the sign of the level-set values,  $\phi$ , are switched accordingly. The multi-layer perceptron then acts on the transformed version of the input stencil and infers the signed  $h\kappa$  at last. As

---

**Algorithm 3:** Hybrid approach to estimating dimensionless mean curvature.

---

**Input:** mesh size,  $h$ ; level-set curvature neural network,  $F_h(\cdot)$ ; nine-point stencil level-set values,  $\phi$ .

**Result:** dimensionless curvature at the interface,  $h\kappa$ .

```
1 estimate  $h\kappa$  using the compound numerical approach;
2 if  $|h\kappa| < h\kappa_{flat}$  then
3   | return  $h\kappa$ ;
4 else
5   | use the numerical estimation of  $h\kappa$  to determine its curvature sign,  $\varsigma$ ;
6   | if  $\varsigma$  is + then
7     |    $\phi \leftarrow -\phi$ ; // Flip sign of stencil level-set values
8   | end
9   |  $\phi \leftarrow \text{Preprocess}(\phi)$ ;
10  |  $h\kappa = F_h(\phi)$ ; // Neural inference
11  | if  $\varsigma$  is + then
12    |    $h\kappa \leftarrow -h\kappa$ ; // Fix inference sign
13  | end
14  | return  $h\kappa$ ;
15 end
```

---

we prove in Section 4, the hybrid approach in Algorithm 3 is more effective in several aspects than using any of its components alone.

A key concept in Algorithm 3 deserving additional explanation is  $\kappa_{flat}$ .  $\kappa_{flat}$  is a positive threshold that triggers the neural network inference and helps discriminate regions where the compound numerical method has proven to work well. In these cases, it is futile to call for a costly neural evaluation to improve numerical accuracy. These savings are especially true if one has never exposed the multi-layer perceptron to samples extracted from near planar or straight-line interfaces. Likewise,  $\kappa_{flat}$  can reduce training complexity because it requires no generation of or learning from data pairs, where the target dimensionless curvature is greater than  $-h\kappa_{flat}$ . However, it is always recommendable to give some room to the maximum expected output values in  $\mathcal{D}$ . In other words,  $\kappa \leq -C\kappa_{flat}$ ,  $\forall(\phi, h\kappa)$ , and  $0 < C < 1$ , so that the neural network can smoothly interpolate curvatures near the upper bound,  $-h\kappa_{flat}$ . In this work, we have chosen  $\kappa_{flat} = 5$  and  $C = \frac{1}{10}$ . For this reason,  $\kappa_{min} = \frac{1}{2}$  in Algorithms 1 and 2, as explained in Sections 3.1 and 3.2.

Training a level-set curvature neural network is algorithmically simpler but much more resource-intensive than any of the tasks described so far. Given a cell width,  $h$ , we design and train the corresponding multi-layer perceptron,  $F_h(\cdot)$ , on the negative-curvature data set,  $\mathcal{D}$ , using TensorFlow [48] and Keras [49] in Python. We follow customary practices [13, 14] and split  $\mathcal{D}$  into training, test, and validation subsets using 70%, 15%, and 15% of the data pairs. As a technical note, we generate all the samples collected in Algorithms 1 and 2 with our in-house C++ implementation of the parallel adaptive level-set method [44]. This implementation also contains tools to realize the compound numerical approach that complements Algorithm 3 and allows us to perform curvature accuracy assessments for any interface.

As seen in Figure 1, the inputs to a curvature neural network are the preprocessed versions of the level-set values in  $\phi$ . Preprocessing is not only crucial during training but also during testing and deployment. The preprocessing mechanism is based on the training subset and is used to transform raw feature vectors into a more suitable representation for the regression model [41]. In particular, as proven by LeCun *et al.* in [50], we have discovered that centering, scaling, and uncorrelating features in  $\phi$  via *principal component analysis* (or PCA) and *whitening* speeds up convergence and delivers better results than typical standardization (see [39]). The idea behind this is to scale uncorrelated centered features to the same level of importance so that the neural estimator can decide more easily which of them to emphasize [13]. In our case, we use SciKit-Learn’s PCA class [41] to perform this transformation and Python’s pickle object serialization to port the transformer across applications.

To conclude this section, we note that our networks for solving the curvature problem exhibit the five-layer architecture already shown in Figure 1. The input and output neurons of the regression models are linear. On the other hand, all the computing nodes at the intermediate, hidden layers are nonlinear ReLU units. We have used TensorFlow’s back-propagation and Adam optimizer to adjust the connection weights and minimize the mean squared error loss function (or MSE) computed off the target values in  $\mathcal{D}$ . Every such weight update takes place after observing a batch of 64 samples. Besides, we monitor the validation subset’s mean absolute error metric (or MAE) for two primary reasons. First, it allows us to stabilize the optimization process by halving the learning rate (which starts at 0.00015) whenever

the MAE does not improve for fifteen epochs. Also, it helps us prevent overfitting by stopping backpropagation if the MAE stagnates for sixty epochs. These aspects, among others, are integrated into the fitting program using Keras’ built-in callback functions. As a final comment, we remark that the hyperparameters just provided have been found to generalize well, irrespective of the domain resolutions studied in section 4. As for the hidden layers’ size, the latter largely depends on  $h$  and the quality of the approximated distances to  $\Gamma$  in  $\phi$ .

#### 4. Experiments and Results

Next, we introduce a few performance tests of the hybrid approach over static, smooth interfaces. First, we provide a detailed comparison between our framework and the compound numerical method in a coarse adaptive grid. This assessment precedes a convergence test where we consider finer local resolutions.

Our tests center on estimating the dimensionless curvature at the zero level-set of the bivariate function

$$\phi_{rose}(x, y) = \sqrt{x^2 + y^2} - a \cos(p\theta) - b, \quad (10)$$

where  $\theta \in [0, 2\pi)$  is the angle of the vector toward  $(x, y)$  with respect to the horizontal, and  $a, b, p$  are shape parameters. The interface  $r(\theta) = a \cos(p\theta) + b$  is commonly referred to in the literature as the “polar rose.” One can determine the curvature along  $\Gamma$  for this simple form with the expression:

$$\kappa_{rose}(\theta) = \frac{r^2(\theta) + 2(r'(\theta))^2 - r(\theta)r''(\theta)}{(r^2(\theta) + (r'(\theta))^2)^{3/2}}. \quad (11)$$

Throughout this section, we set  $p = 5$ . Varying  $a$  and  $b$  thus determines how steeply the rose bends each of its five petals. For clarity, we restate that the training and testing samples coming from reinitialized level-sets have been computed with ten iterations for reshaping  $\phi_{rls}^c, \phi_{rls}^s$ , and  $\phi_{rose}$  into signed distance functions.

##### 4.1. Evaluation in a Low-Resolution Grid

In their prior research [39], Larios and Gibou hinted at incorporating machine learning for helping the level-set method to handle under-resolved regions and steep curvatures in low resolutions. Here, we realize that idea and apply our hybrid approach to estimating dimensionless curvature in a relatively coarse adaptive grid.

Let  $\Omega$  be a non-periodic computational domain discretized into an adaptive p4est macromesh [42, 51]. Further, let  $\ell_{max} \in \mathbb{N}$  be the maximum level of refinement of each of the  $1 \times 1$  macrocells or quadtrees [45] that compose  $\Omega$ . The recursive subdivision of quadtree cells down to the finest local resolution next to  $\Gamma$  abides by the splitting criterion proposed by [43]:

$$\min_{v \in \mathcal{V}(c)} |\phi(v)| \leq \text{Lip}(\phi(v)) \times \text{diag}_\ell(c), \quad (12)$$

where  $\mathcal{V}$  is the set of vertices in cell  $c$ ,  $\text{diag}_\ell(c)$  is its diagonal length (at the corresponding level  $\ell < \ell_{max}$ ), and  $\text{Lip}(\phi(v))$  is the Lipschitz constant for the level-set function (set to 1.2 for all cells).

By defining  $\ell_{max} = 7$ , we get a minimum, uniform local mesh size  $h = 1/128$ . We have trained a suitable curvature neural network,  $F_{hyb}^{(7)}(\cdot)$ , for this spacing with 2’330,785 samples extracted from circular- and sinusoidal-interface level-sets in the negative curvature spectrum,  $-85\frac{1}{3} \leq \kappa \leq -\frac{1}{2}$ . The optimal multilayer perceptron for this case study has four hidden layers with 180 ReLU units each (refer to Figure 1). Such an architecture added up to 99,721 parameters among weight matrices and biases. Figure 4b compares the fitting quality of the neural network and the compound numerical method over a data set  $\mathcal{D}_{rls}$ . This set contains pairs  $(\phi, h\kappa)$ , where  $\phi$  is a stencil of reinitialized level-set values. Also, note that non-overlapping portions of  $\mathcal{D}_{rls}$  were used in the training, test, and validation subsets of  $\mathcal{D}$ . Figure 4b summarizes the training outcome by considering those samples that mirror a practical scenario where only reinitialized level-set information is available. A quick inspection of the plots in Figure 4 reveals the superior accuracy of our regression model and confirms that machine learning works better when  $|\kappa|$  is large. Table 1 supplements these results with some error statistics over  $\mathcal{D}_{rls}$  regarding the raw mean curvature,  $\kappa$ . The difference between both approaches is surely drastic.

We first test  $F_{hyb}^{(7)}$  and the hybrid inference approach outlined in Algorithm 3 on  $\phi_{rose}(x, y)$ . Let  $a = 0.075$  and  $b = 0.35$ . These shape parameters define a five-petaled smooth interface,  $\Gamma_1$ , as seen in Figure 5a. Then, we discretize the square computational domain  $\Omega \equiv [-0.5, +0.5]^2$  with a single quadtree with  $\ell_{max} = 7$ , which produces a minimum

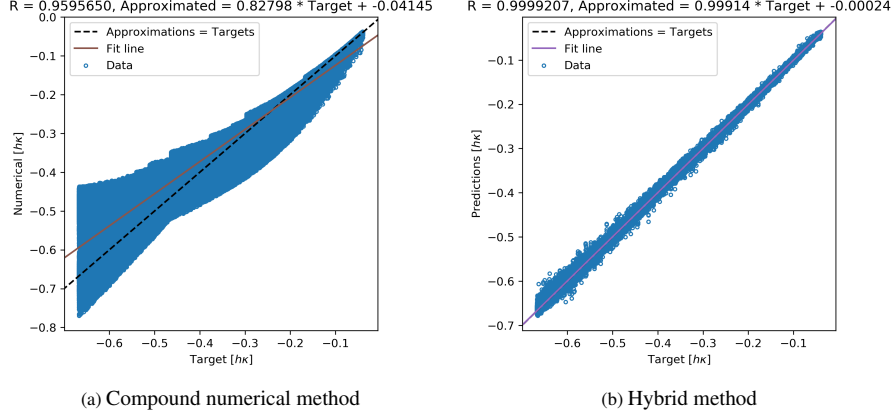


Figure 4: Training outcome correlation between expected and approximated  $hk$  over  $\mathcal{D}_{rls}$  in an adaptive grid with  $\ell_{max} = 7$ .

spacing of  $h = 1/128$ . These settings allow us to gather 632 data pairs for which we can calculate their mean curvature exactly with equation (11) at their closest points on  $\Gamma_1$ . Similar to locating nearest points to vertices along sine waves (section 3.2), we use bisection followed by Newton-Raphson’s root finding to determine the optimal angle,  $\theta^*$ , that yields  $\mathbf{x}_{i,j}^\perp$  in Figure 2. In addition, we keep the network threshold  $\kappa_{flat} = 5$ , as stated in section 3.3.

Figure 6 illustrates the quality of the dimensionless curvature estimations computed with our hybrid approach and the compound numerical method. For reference, we also include the numerical approximations when we reinitialize  $\phi_{rose}$  with 20 iterations. It is then easy to see that our strategy delivers comparable or better results than the conventional numerical schemes when the interface features slowly varying curvatures. Table 2 has more to say about this. It provides raw  $\kappa$  error statistics and shows that our framework is slightly more accurate in the  $L^\infty$  norm. The latter holds even if one uses numerical procedures alone with twice the number of redistancing operations necessary for training  $F_{hyb}^{(7)}$ . Last, Table 2 tells us that, on average, the numerical method gets better at estimating  $\kappa$  as the number of iterations increases. This behavior is expected, but the gained advantage is not significant if we contrast it with the mean absolute error incurred by the hybrid algorithm.

	Mean Absolute Error	Max Absolute Error	Mean Squared Error
Neural network	$1.815692 \times 10^{-1}$	7.242649	$8.291462 \times 10^{-2}$
Compound numerical method	4.511332	$2.926552 \times 10^1$	$5.141757 \times 10^1$

Table 1: Training outcome statistics with respect to  $\kappa$  over  $\mathcal{D}_{rls}$  in an adaptive grid with  $\ell_{max} = 7$ .

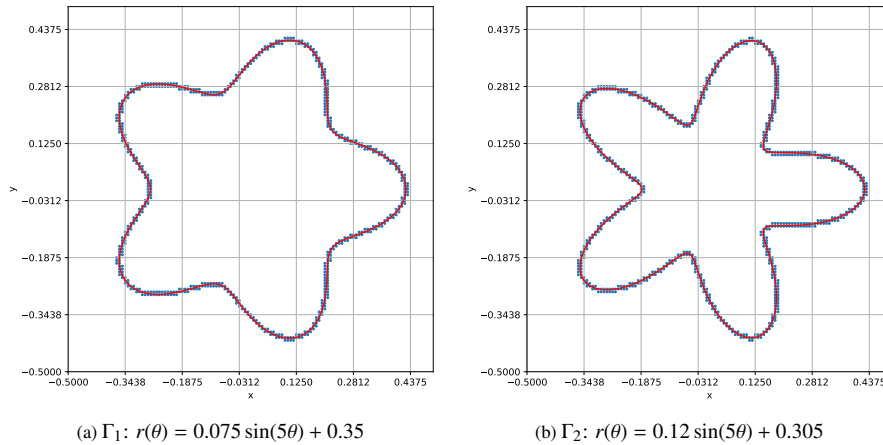


Figure 5: Two shape configuration of the polar rose interface. The continuous line denotes the interface, and the dots indicate samples collected next to  $\Gamma$ .

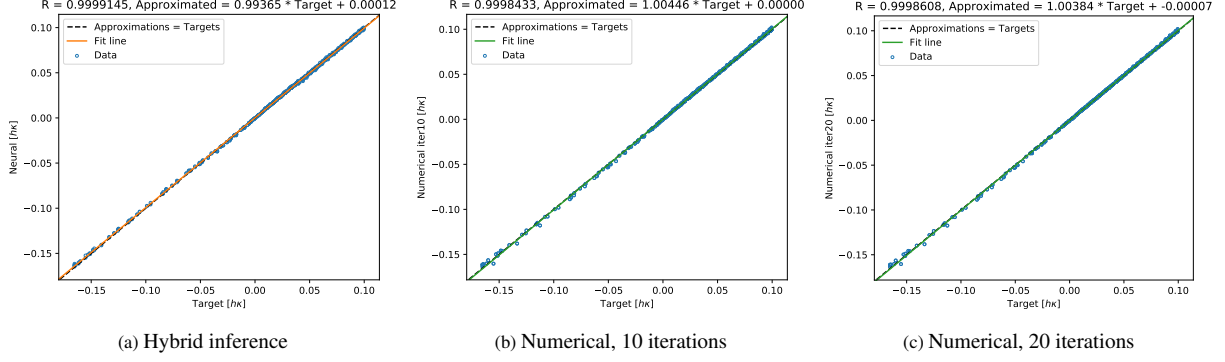


Figure 6: Correlation between expected and approximated  $h\kappa$  using the hybrid approach and the compound numerical method on  $\Gamma_1$  in an adaptive grid with  $\ell_{max} = 7$ .

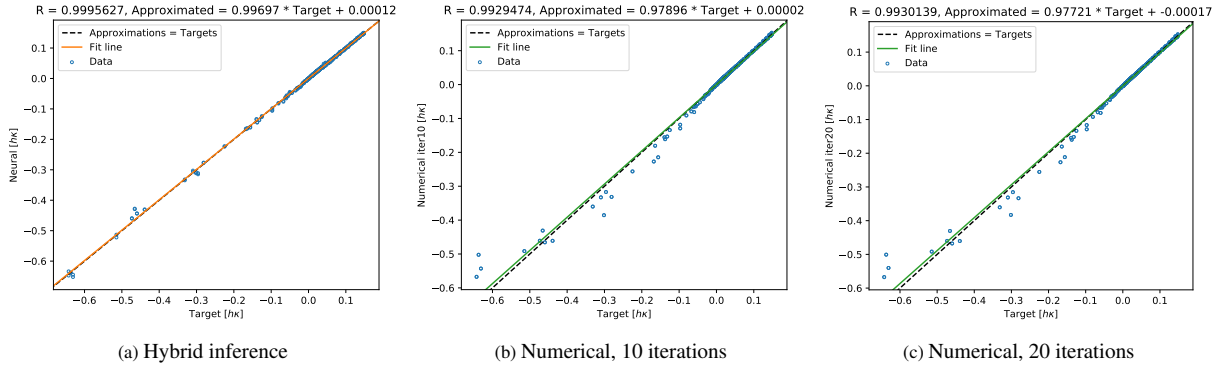


Figure 7: Correlation between expected and approximated  $h\kappa$  using the hybrid approach and the compound numerical method on  $\Gamma_2$  in an adaptive grid with  $\ell_{max} = 7$ .

In a second test, we consider the function in equation (10) with  $a = 0.12$  and  $b = 0.305$ . This configuration is characterized by a zero level set,  $\Gamma_2$ , that displays steeper concave regions than  $\Gamma_1$ , as seen in Figure 5b. The experiment setup is similar to the previous case study, except that the number of samples collected along the interface is 740. Figure 7 shows the correlation plots obtained with our hybrid approach and the compound numerical method alone. For reference, we include again the numerical estimations attained with 20 redistancing operations.

Comparing Figures 6 and 7 reveals that  $\Gamma_2$  is more challenging to deal with, given the relatively coarse mesh discretization. Both methods struggle, but the hybrid approach is by far superior at handling steep curvatures regardless of the number of iterations used to reinitialize  $\phi_{rose}$ . Table 3 summarizes these results more succinctly. It shows that the hybrid strategy is up to 3.5 times more accurate in the  $L^\infty$  norm and incurs as much as 44% of the mean absolute error in the traditional numerical method. Unlike [39], the gains in robustness and correctness are quite significant when one integrates a greater diversity of training samples to optimize a curvature regression model.

#### 4.2. Convergence Study

We now study the behavior of the hybrid framework as  $h \rightarrow 0$  on the irregular interface  $\Gamma_2$ . We have chosen this interface configuration because of its challenging steep concave regions. To measure our strategy's performance objectively, we compare it with each of its components alone. More clearly, we consider a network-only inference

Method	Mean Absolute Error	Max Absolute Error	Mean Squared Error
Hybrid approach	$8.559648 \times 10^{-2}$	$4.765949 \times 10^{-1}$	$1.298467 \times 10^{-2}$
Numerical method, 10 iters.	$9.129319 \times 10^{-2}$	$6.847077 \times 10^{-1}$	$2.099346 \times 10^{-2}$
Numerical method, 20 iters.	$7.665316 \times 10^{-2}$	$6.701565 \times 10^{-1}$	$1.833753 \times 10^{-2}$

Table 2: Error analysis with respect to  $\kappa$  for  $\Gamma_1$  in an adaptive grid with  $\ell_{max} = 7$ .

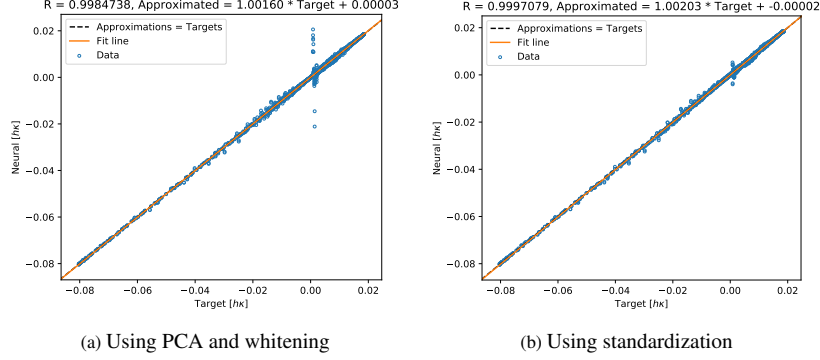


Figure 8: Comparison of the generalization behavior of the network-only model for  $\nu = 10$  when inferring the dimensionless curvature along  $\Gamma_2$ .

system (as in [36, 37, 39]), the conventional compound numerical method, and the hybrid model introduced in section 3.3.

The convergence analysis realizes the idea of building independent neural networks for each grid resolution. This study agrees with the thesis that a dictionary of level-set curvature neural networks is simpler and more accurate than a universal regression model. Therefore, we have trained suitable models,  $F_{net}^{(\nu)}$  and  $F_{hyb}^{(\nu)}$ , for the network-only and hybrid strategies from circular- and sinusoidal-interface samples in four resolutions,  $h_\nu = 2^{-\nu}$ , where  $\nu = 7, 8, 9, 10$ . To assemble the corresponding learning data sets  $\mathcal{D}^{(\nu)}$ , we consistently use  $\kappa_{min} = 0.5$ ,  $\kappa_{max} = 85\frac{1}{3}$ , and  $\kappa_{flat} = 5$ , as described in sections 3.1 and 3.2. Regarding Algorithm 3, however, we opt for redefining the inference threshold  $\kappa_{flat}^{(\nu)} = (\nu - 6)\kappa_{flat}$ , so that the curvature solver prefers the numerical method over the neural network in wider curvature intervals around 0 as  $\nu \rightarrow 10$ . The goal is to leverage the traditional numerical framework, knowing that its accuracy increases as the mesh becomes finer.

As a prelude to the accuracy convergence study, we begin by analyzing the architectural complexity of  $F_{net}^{(\nu)}$  and  $F_{hyb}^{(\nu)}$ . Table 4 shows the relation among mesh size, number of trainable parameters, and number of computing units in each of the models' four hidden layers. It also includes the cardinality of  $\mathcal{D}^{(\nu)}$  and a couple of test-subset curvature error statistics.

There are a few points in Table 4 worth discussing. As noted above, network-only models must account for the full curvature spectrum; thus,  $F_{net}^{(\nu)}$  required exposure to both positive and negative curvature samples. Some direct consequences of this were longer training times and more complex architectures than  $F_{hyb}^{(\nu)}$ .

A second observation drawn from Table 4 concerns the lack of correlation between the minimum cell width and the size of the hidden layers in  $F_{net}^{(\nu)}$ . We attribute such a disassociation to the need for sufficient neural capacity to keep up with the increasing variety of sample patterns as  $h \rightarrow 0$ . Also, deciding on the hidden layer size was mostly arbitrary; most times, we settled on the shown architectures after several trials. Even though we sought to simplify all neural topologies as much as possible, it turned out to be easier to design  $F_{hyb}^{(\nu)}$  than tweaking the hyperparameters for  $F_{net}^{(\nu)}$ .

Last, we reflect on the seemingly amiss statistics for  $\nu = 10$  in Table 4. All neural networks up to  $\nu = 9$  used principal component analysis and whitening to transform the input vector  $\phi$ , as described in section 3.3. However, when we optimized  $F_{net}^{(10)}$  with the same input transformation, the generalization performance on  $\Gamma_2$  degraded significantly along regions where  $h\kappa \sim 0$  (see Figure 8a). The problem persisted in different network configurations and despite  $\kappa$  average squared and absolute errors around  $1.9 \times 10^{-3}$  and  $3.1 \times 10^{-2}$ , respectively, in the test subset. After further

Method	Mean Absolute Error	Max Absolute Error	Mean Squared Error
Hybrid approach	$1.778957 \times 10^{-1}$	4.841265	$1.601629 \times 10^{-1}$
Numerical method, 10 iters.	$4.441347 \times 10^{-1}$	$1.726560 \times 10^1$	2.570065
Numerical method, 20 iters.	$4.046386 \times 10^{-1}$	$1.745362 \times 10^1$	2.554465

Table 3: Error analysis with respect to  $\kappa$  for  $\Gamma_2$  in an adaptive grid with  $\ell_{max} = 7$ .

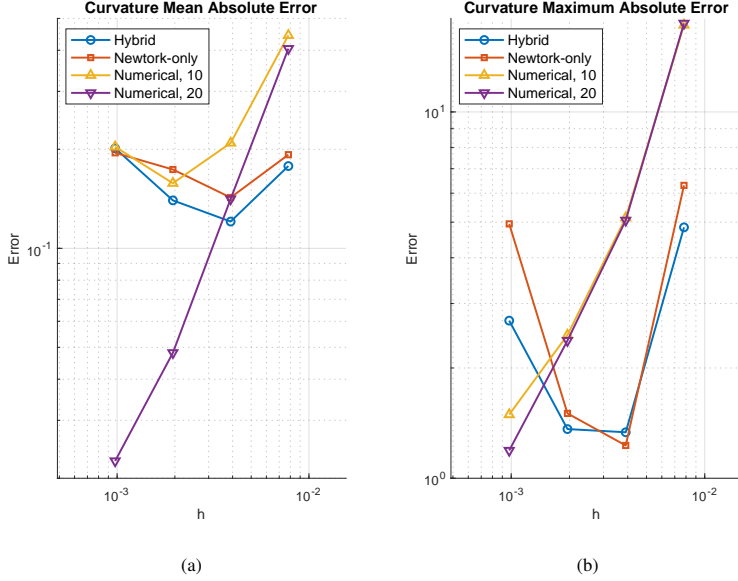


Figure 9: Curvature estimation accuracy in the (a)  $L^1$  and (b)  $L^\infty$  norms using the proposed hybrid approach, a network-only framework as in [36, 37, 39], and the compound numerical method with 10 and 20 iterations to reinitialize  $\phi_{rose}$ .

investigation, we found that typical standardization<sup>2</sup> helped produce more accurate curvature estimations for stencils not included in  $\mathcal{D}^{(10)}$  (see Figure 8b). There is still no sound explanation for this phenomenon, but overfitting probably caused such a pathological behavior. This issue could have been also exacerbated by the fast training convergence due to whitening. For these reasons, we have incorporated  $F_{net}^{(10)}$  optimized for normalized level-set values, similar to the usage reported in [39].

Next, we assess the quality of the mean curvature approximations along  $\Gamma_2$  at various resolutions. Like in section 4.1, we start by discretizing the computational domain with an adaptive grid. The domain macromesh comprises a single  $1 \times 1$  quadtree with a maximum level of refinement  $\ell_{max}^\nu = \nu$ . Also, we note that both  $F_{hyb}^{(\nu)}$  and  $F_{net}^{(\nu)}$  operate only on level-set values reinitialized with ten iterations. For reference, we include results from using 20 iterations, but just with the compound numerical approach.

Figure 9 summarizes the curvature estimation convergence behavior of the proposed hybrid inference system. Tables 5 and 6, along with Table 3, provide a more detailed  $\kappa$  error analysis. When contrasted with the compound numerical method, our approach is superior in the error  $L^\infty$  norm, particularly in low resolutions, i.e.,  $\nu = 7, 8, 9$ . The hybrid framework even outperforms the conventional numerical schemes involving twice the number of operations to

<sup>2</sup>Preprocessing inputs with SciKit-Learn’s `StandardScaler` object.

$\nu$	Approach	$ \mathcal{D}^{(\nu)} $	Parameters	Units per Hidden Layer	Test MSE	Test MAE
7	Network-only	4’442,728	200,193	256	$7.862888 \times 10^{-2}$	$1.688352 \times 10^{-1}$
	Hybrid	2’330,785	99,721	180	$6.641488 \times 10^{-2}$	$1.576492 \times 10^{-1}$
8	Network-only	7’258,628	159,145	228	$1.377657 \times 10^{-2}$	$7.653323 \times 10^{-2}$
	Hybrid	3’629,297	89,081	170	$1.183376 \times 10^{-2}$	$7.074739 \times 10^{-2}$
9	Network-only	9’315,620	148,281	220	$4.523646 \times 10^{-3}$	$4.539807 \times 10^{-2}$
	Hybrid	5,205,788	52,521	130	$5.544708 \times 10^{-3}$	$5.118205 \times 10^{-2}$
10	Network-only	12’592,164	159,145	228	$1.097944 \times 10^{-2}$	$7.300141 \times 10^{-2}$
	Hybrid	6,273,339	31,401	100	$3.042110 \times 10^{-3}$	$4.051211 \times 10^{-2}$

Table 4: Topological analysis and test error statistics for network-only and hybrid approaches.

reinitialize the level-set in equation (10). Regarding average correctness, the hybrid algorithm is also more accurate than, if not comparable to, the numerical method whenever  $\phi_{rose}$  gets reinitialized with ten iterations. In like manner, Figure 9a demonstrates that the neural networks and the numerical method based on 10-iteration reinitialization converge to the same accuracy as the mesh size decreases. As expected, when one uses 20 operations for redistancing and  $h \leq 2^{-9}$ , the numerical precision is higher in the  $L^1$  norm.

Figure 9 further shows that our proposed strategy is more accurate than  $F_{net}^{(\nu)}$  in nearly all tested resolutions in both error metrics. By combining these results with the information in Table 4, it is evident that the hybrid solver is more efficient than the network-only inference system. Indeed, the hybrid mechanism’s main advantage is that it needs much fewer computing units to attain the same or better accuracy than the full curvature model.

Unlike the compound numerical method, none of the neural network strategies here tested exhibits a definite convergence order. Qi *et al.* have corroborated this datum in their study of machine learning and VOF [36]. In particular, our experiments show that it gets increasingly complicated and quite resource-intensive to train either  $F_{net}^{(\nu)}$  or  $F_{hyb}^{(\nu)}$  as  $h_\nu \rightarrow 0$ . Even with enormous data sets  $\mathcal{D}^{(\nu)}$ , there is a latent risk of running into overfitting, as seen in Figure 8a. Overall, optimizing neural models to estimate curvature in the level-set method is a cumbersome process for extremely small grid spacings. In that case, it is rather convenient to rely on traditional numerical schemes; they are less expensive and deliver more accurate and predictable approximations than curvature solvers based on neural models.

## 5. Conclusions

We have presented a deep-learning-based hybrid approach for the estimation of mean curvature in the level-set method<sup>3</sup>. Our hybrid inference system builds on the concept of curvature regression models introduced in [39]. To improve these models’ accuracy, we fit them to richer data sets constructed from circular- and sinusoidal-interface samples. The core of our framework is a switching mechanism that relies on conventional numerical schemes to gauge curvature. If the curvature magnitude is larger than a resolution-dependent threshold, it then uses a neural network to deliver a better  $h\kappa$  approximation. Such a network does not need to be trained on the whole curvature spectrum, leading to more compact architectures, enhanced data exploitation, and faster parameter adaptation.

Our experiments have shown that the hybrid strategy is more accurate than the compound numerical method and more efficient than full-curvature neural networks. In particular, the hybrid inference system yields remarkable gains in precision when dealing with coarse grids and when the interfaces exhibit pronounced concave or convex regions. As resolution increases, however, we have observed some deterioration in neural correctness. This unexpected result has been consistent in both the hybrid and the compatible full-curvature model, as reported in section 4.2. We think the issue is probably a consequence of overfitting, which gets exacerbated by using principal component analysis and whitening to treat data inputs. Thus, further research on this pathologic behavior is required to understand how to design data sets effectively for training in high resolutions.

<sup>3</sup>Our level-set curvature neural networks are available at <https://github.com/UCSB-CASL/HybridDLCurvature>.

$\nu$	Hybrid	Order	Network-Only	Order	Numerical 10 Iterations	Order	Numerical 20 Iterations	Order
8	$1.206242 \times 10^{-1}$	0.56	$1.427076 \times 10^{-1}$	0.43	$2.090196 \times 10^{-1}$	1.09	$1.412793 \times 10^{-1}$	1.52
9	$1.399002 \times 10^{-1}$	-0.21	$1.736572 \times 10^{-1}$	-0.28	$1.577540 \times 10^{-1}$	0.41	$4.813345 \times 10^{-2}$	1.55
10	$2.013844 \times 10^{-1}$	-0.53	$1.951764 \times 10^{-1}$	-0.17	$2.035428 \times 10^{-1}$	-0.37	$2.257036 \times 10^{-2}$	1.09

Table 5: Convergence analysis with respect to  $\kappa$  mean absolute error ( $L^1$  norm) in  $\Gamma_2$  at different resolutions.

$\nu$	Hybrid	Order	Network-Only	Order	Numerical 10 Iterations	Order	Numerical 20 Iterations	Order
8	1.335202	1.86	1.228807	2.36	5.141835	1.75	5.059004	1.79
9	1.362297	-0.03	1.503125	-0.29	2.460210	1.06	2.375857	1.09
10	2.693102	-0.98	4.947860	-1.72	1.492015	0.72	1.190646	1.00

Table 6: Convergence analysis with respect to  $\kappa$  maximum absolute error ( $L^\infty$  norm) in  $\Gamma_2$  at different resolutions.

The hybrid inference algorithm and its corresponding curvature neural networks are part of our long-term plan to develop a family of level-set machine learning methods. With this goal in mind, we have reserved the coupling of the hybrid strategy with a full-fledged simulation for upcoming work. This will help assess the response of our improved regression models to level-set functions subject to advection and reinitialization. Also, a subordinate task to such a real simulation will require the migration of the inference system from TensorFlow/Keras to C++. Després and Jourden have already done so with their VOF-machine-learning schemes in [35] with the aid of `keras2cpp` [52]. We believe the same approach is promising for our future developments, alongside network pruning to reduce evaluation times [53, 54].

## Acknowledgement

Use was made of computational facilities purchased with funds from the National Science Foundation (CNS-1725797) and administered by the Center for Scientific Computing (CSC). The CSC is supported by the California NanoSystems Institute and the Materials Research Science and Engineering Center (MRSEC; NSF DMR 1720256) at UC Santa Barbara.

## References

- [1] A. Friedman. *Variational Principles of Free-Boundary Problems*. Dover Publications, 2010.
- [2] S. Popinet. Numerical Models of Surface Tension. *Annu. Rev. Fluid Mech.*, 50(1):49–75, January 2018.
- [3] M. Sussman, P. Smereka, and S. Osher. A Level Set Approach for Computing Solutions to Incompressible Two-Phase Flow. *J. Comput. Phys.*, 114(1):146–159, September 1994.
- [4] M. Sussman, E. Fatemi, P. Smereka, and S. Osher. An Improved Level Set Method for Incompressible Two-Phase Flows. *Comput. & Fluids*, 27(5-6):663–680, June 1998.
- [5] T. Chan and L. Vese. Active Contour Without Edges. *IEEE Trans. on Image Process.*, 10:266–277, 2001.
- [6] M. Theillard, F. Gibou, and T. Pollock. A Sharp Computational Method for the Simulation of the Solidification of Binary Alloys. *J. Sci. Comput.*, 63:330–354, 2015.
- [7] M. A. Alias and P. R. Buenzli. A Level-Set Method for the Evolution of Cells and Tissue During Curvature-Controlled Growth. *Int. J. Numer. Methods Biomed. Eng.*, 36(1):e3279, January 2020.
- [8] S. Osher and J. A. Sethian. Fronts Propagating with Curvature Dependent Speed: Algorithms Based on Hamilton-Jacobi Formulations. *J. Comput. Phys.*, 79(1):12–49, 1988.
- [9] S. Osher and R. Fedkiw. *Level Set Methods and Dynamic Implicit Surfaces*, volume 153 of *Applied Mathematical Sciences*. Springer-Verlag, 2002. New York, NY.
- [10] F. Gibou, R. Fedkiw, and S. Osher. A Review of Level-Set Methods and Some Recent Applications. *J. Comput. Phys.*, 353:82–109, 2018.
- [11] C. W. Hirt and B. D. Nichols. Volume of Fluid (VOF) Method for the Dynamics of Free Boundaries. *J. Comput. Phys.*, 39:201–225, 1981.
- [12] R. Brawun and M. Murray. Adaptive Phase-Field Computations of Dendritic Crystal Growth. *J. Cryst. Growth*, 174:41, 1997.
- [13] C. C. Aggarwal. *Neural Networks and Deep Learning – A Textbook*. Springer, 2018.
- [14] P. Mehta, M. Bukov, C. Wang, A. G. R. Day, C. Richardson, C. K. Fisher, and D. J. Schwab. A High-Bias, Low-Variance Introduction to Machine Learning for Physicists. *Phys. Rep.*, 810:1–124, May 2019.
- [15] A. Gerón. *Hands-on Machine Learning with Scikit-Learn, Keras & TensorFlow: Concepts, Tools, and Techniques to Build Intelligent Systems*. O’Reilly, second edition, November 2019.

- [16] T. A. Ngo, Z. Lu, and G. Carneiro. Combining Deep Learning and Level Set for the Automated Segmentation of the Left Ventricle of the Heart from Cardiac Cine Magnetic Resonance. *Medical Image Analysis*, 35:159–171, January 2017.
- [17] T. H. N. Le, K. G. Quach, K. Luu, C. N. Duong, and M. Savvides. Reformulating Level Sets as Deep Recurrent Neural Network Approach to Semantic Segmentation. *IEEE Trans. on Image Process.*, 27(5):2393–2407, May 2018.
- [18] A. Krizhevsky, I. Sutskever, and G. Hinton. Imagenet Classification with Deep Convolutional Neural Networks. In *NIPS Conference*, pages 1097–1105, 2012.
- [19] K. He, X. Zhang, S. Ren, and J. Sun. Deep Residual Learning for Image Recognition. In *CVPR*, pages 770–778, 2016.
- [20] P. Vincent, H. Larochelle, I. Lajoie, Y. Bengio, and P.-A. Manzagol. Stacked Denoising Autoencoders: Learning Useful Representations in a Deep Network with a Local Denoising Criterion. *J. Mach. Learn. Res.*, 11:3371–3408, December 2010.
- [21] I. Goodfellow, J. Pouget-Abadie, M. Mirza, B. Xu, D. Warde-Farley, S. Ozair, A. Courville, and Y. Bengio. Generative Adversarial Nets. In Z. Ghahramani, M. Welling, C. Cortes, N. D. Lawrence, and K. Q. Weinberger, editors, *NeurIPS 27*, pages 2672–2680. Curran Associates, Inc., 2014.
- [22] T. Mikolov, I. Sutskever, K. Chen, G. S. Corrado, and J. Dean. Distributed Representations of Words and Phrases and their Compositionality. In C. J. C. Burges, L. Bottou, M. Welling, Z. Ghahramani, and K. Q. Weinberger, editors, *NeurIPS 26*, pages 3111–3119. Curran Associates, Inc., 2013.
- [23] P. Bojanowski, E. Grave, A. Joulin, and T. Mikolov. Enriching Word Vectors with Subword Information. In *Trans. Assoc. Comput. Linguist.*, volume 5, pages 135–146, 2017.
- [24] M. E. Peters, M. Neumann, M. Iyyer, M. Gardner, C. Clark, K. Lee, and L. Zettlemoyer. Deep Contextualized Word Representations. In *Proc. of NAACL*, 2018.
- [25] S. Arora, Y. Liang, and T. Ma. A Simple but Tough-to-Beat Baseline for Sentence Embeddings. In *ICLR*, April 2017.
- [26] K. Cho, B. V. Merriënboer, Ç. Gülçehre, D. Bahdanau, F. Bougares, H. Schwenk, and Y. Bengio. Learning Phrase Representations Using RNN Encoder-Decoder for Statistical Machine Translation. In *EMNLP*, 2014.
- [27] A. Vaswani, N. Shazeer, N. Parmar, J. Uszkoreit, L. Jones, A. N. Gomez, Ł. Kaiser, and I. Polosukhin. Attention is All you Need. In I. Guyon, U. V. Luxburg, S. Bengio, H. Wallach, R. Fergus, S. Vishwanathan, and R. Garnett, editors, *NeurIPS 30*, pages 5998–6008. Curran Associates, Inc., 2017.
- [28] N. Yadav, A. Yadav, and M. Kumar. *An Introduction to Neural Network Methods for Differential Equations*. SpringerBriefs in Applied Sciences and Technology: Computational Intelligence. Springer, 2015.
- [29] I. E. Lagaris, A. Likas, and D. I. Fotiadis. Artificial Neural Networks for Solving Ordinary and Partial Differential Equations. *IEEE Trans. Neural Netw.*, 9(5):987–1000, 1998.
- [30] I. E. Lagaris, A. C. Likas, and D. G. Papageorgiou. Neural-Network Methods for Boundary Value Problems with Irregular Boundaries. *IEEE Trans. Neural Netw.*, 11(5):1041–1049, September 2000.
- [31] M. Raissi, P. Perdikaris, and G. Karniadakis. Physics Informed Deep Learning (Part I): Data-Driven Solution of Nonlinear Partial Differential Equations. *ArXiv*, abs/1711.10561, 2017.
- [32] M. Raissi. Deep Hidden Physics Models: Deep Learning of Nonlinear Partial Differential Equations. *J. Mach. Learn. Res.*, 19(25):1–24, 2018.
- [33] D. Ray and J. S. Hesthaven. An Artificial Neural Network as a Troubled-Cell Indicator. *J. Comp. Phys.*, 367:166–191, April 2018.

- [34] N. R. Morgan, S. Tokareva, X. Liu, and A. D. Morgan. A Machine Learning Approach for Detecting Shocks with High-Order Hydrodynamic Methods. *AIAA SciTech Forum*, January 2020.
- [35] B. Després and H. Jourden. Machine Learning Design of Volume of Fluid Schemes for Compressible Flows. *J. Comput. Phys.*, 408(1):109275, May 2020.
- [36] Y. Qi, J. Lu, R. Scardovelli, S. Zaleski, and G. Tryggvason. Computing Curvature for Volume of Fluid Methods Using Machine Learning. *J. Comput. Phys.*, 377:155–161, 2019.
- [37] H. V. Patel, A. Panda, J. A. M. Kuipers, and E. A. J. F. Peters. Computing Interface Curvature from Volume Fractions: A Machine Learning Approach. *Comput. & Fluids*, 193:104263, October 2019.
- [38] M. Ataei, M. Bussmann, V. Shaayegan, F. Costa, S. Han, and C. B. Park. NPLIC: A Machine Learning Approach to Piecewise Linear Interface Construction. <https://arxiv.org/abs/2007.04244>, January 2021.
- [39] L. A. Larios-Cárdenas and F. Gibou. A Deep Learning Approach for the Computation of Curvature in the Level-Set Method. *SIAM J. Sci. Comput.*, to appear, January 2021. <https://arxiv.org/abs/2002.02804>.
- [40] C. Min. On Reinitializing Level Set Functions. *J. Comp. Phys.*, 229(8):2764–2772, April 2010.
- [41] F. Pedregosa, G. Varoquaux, A. Gramfort, V. Michel, B. Thirion, O. Grisel, M. Blondel, P. Prettenhofer, R. Weiss, V. Dubourg, J. Vanderplas, A. Passos, D. Cournapeau, M. Brucher, M. Perrot, and E. Duchesnay. Scikit-learn: Machine Learning in Python. *J. Mach. Learn. Res.*, 12:2825–2830, 2011.
- [42] J. Strain. Tree Methods for Moving Interfaces. *J. Comput. Phys.*, 151(2):616–648, May 1999.
- [43] C. Min and F. Gibou. A Second Order Accurate Level Set Method on Non-Graded Adaptive Cartesian Grids. *J. Comput. Phys.*, 225(1):300–321, July 2007.
- [44] M. Mirzadeh, A. Guittet, C. Burstedde, and F. Gibou. Parallel Level-Set Methods on Adaptive Tree-Based Grids. *J. Comput. Phys.*, 322:345–364, 2016.
- [45] M. de Berg, M. van Kreveld, M. Overmars, and O. Schwarzkopf. *Computational Geometry - Algorithms and Applications*. Springer, second edition, 2000.
- [46] R. Parent. *Computer Animation: Algorithms and Techniques*. Morgan Kaufmann, second edition, 2008.
- [47] Jr. F. S. Hill. *Computer Graphics Using OpenGL*. Prentice-Hall Inc., second edition, 2001.
- [48] M. Abadi, A. Agarwal, P. Barham, E. Brevdo, Z. Chen, C. Citro, G. S. Corrado, A. Davis, J. Dean, M. Devin, S. Ghemawat, I. Goodfellow, A. Harp, G. Irving, M. Isard, R. Jozefowicz, Y. Jia, L. Kaiser, M. Kudlur, J. Levenberg, D. Mané, M. Schuster, R. Monga, S. Moore, D. Murray, C. Olah, J. Shlens, B. Steiner, I. Sutskever, K. Talwar, P. Tucker, V. Vanhoucke, V. Vasudevan, F. Viégas, O. Vinyals, P. Warden, M. Wattenberg, M. Wicke, Y. Yu, and X. Zheng. TensorFlow: Large-Scale Machine Learning on Heterogeneous Systems, 2015.
- [49] F. Chollet et al. Keras. <https://keras.io>, 2015.
- [50] Y. A. LeCun, L. Bottou, G. B. Orr, and K.-R. Müller. *Efficient BackProp*, volume 7700 of *Lecture Notes in Comput. Sci.*, pages 9–48. Springer Berlin Heidelberg, Berlin, Heidelberg, 2012.
- [51] C. Burstedde, L. C. Wilcox, and O. Ghattas. p4est: Scalable Algorithms for Parallel Adaptive Mesh Refinement on Forests of Octrees. *SIAM J. Sci. Comput.*, 33(3):1103–1133, 2011.
- [52] P. Płoński. keras2cpp. <https://github.com/pplonski/keras2cpp>, December 2020.
- [53] M. Zhu and S. Gupta. To Prune, or Not to Prune: Exploring the Efficacy of Pruning for Model Compression. In *ICLR Workshop*, 2018.
- [54] J. Frankle and M. Carbin. The Lottery Ticket Hypothesis: Finding Sparse, Trainable Neural Networks. <https://arxiv.org/abs/1803.03635>, 2019.